GEOMATICS AND ENVIRONMENTAL ENGINEERING • Volume 20 • Number 3 • 2026

https://doi.org/10.7494/geom.2026.20.3.105

Drought Assessment and Forecasting according to the Köppen–Geiger Climate Classification Using GRACE and MERRA Observations

Monika Birylo

University of Warmia and Mazury in Olsztyn, Faculty of Geoengineering, Olsztyn, Poland

Abstract: Prolonged and recurrent droughts are a problem of the 21st century. Agriculture, grazing, fires, logging, and mining make soil susceptible to permanent degradation. However, well-managed land can recover from long drought cycles. Because drought is increasingly affecting larger areas, continuous monitoring and risk assessment are essential. Satellite-based models provide global observations of the Earth and enable their assessment using indices, thereby supporting the classification of the examined areas. In this study, the Combined Climatological Deviation Index (CCDI) and the Water Storage Deficit Index (WSDI) were calculated to evaluate drought sensitivity in Europe, within its climatic zones according to the Köppen–Geiger classification. Based on the research, it was concluded that almost all areas show a tendency towards drying, and the predictions indicate that the current drought conditions and their pace will continue. The CCDI and WSDI are very useful in studies of drought in Europe.

Keywords: total water storage, precipitation, drought, WSDI, CCDI

Received: October 15, 2025; accepted: March 5, 2026

E-mail and ORCID iD: monika.sienkiewicz@uwm.edu.pl, https://orcid.org/0000-0002-8006-288X.

1. Introduction

The rationale for addressing this topic is the rapidly progressing climate crisis, which is currently intensifying through dry conditions, including agricultural drought, declining drinking water resources, drying water reservoirs due to very high summer temperatures, and year-round rainfall deficits. These problems are discussed particularly often in southern Europe; however, it is also important to consider the whole of Europe and compare the state of water resources across its regions. Drought is a serious environmental problem widely discussed in the scientific literature. This phenomenon is related to soil degradation in dry areas of the Earth. In the context of climate change, it becomes important to constantly monitor and understand the causes of drought, as well as its severity and impacts on people and the environment. This is particularly important for agriculture and food security. Estimates published in 2020 indicated that over 50% of arid regions are at risk of desertification, due to persistent drought [1]. The United Nations, through the Convention to Combat Desertification (UNCCD), has estimated an annual loss of 12 million hectares of land due to soil drying. This area corresponds to a loss of 20 million tons of cereal production [2].

Generally, prolonged periods of precipitation lead to drought, a major environmental hazard. A second major driver is anomalously high temperature. Drought is divided into meteorological drought (caused by low precipitation and high temperature), hydrological drought (caused by low water levels in basins and declining stream flow), agricultural drought (caused by high temperature, increased evapotranspiration, and low soil moisture), and socio-economic drought (caused by water scarcity, food insecurity, and health issues).

The progression of drought types is as follows: initially, meteorological drought occurs, then agricultural drought, which causes hydrological drought, and finally socio-economic drought. The causes of drought may be divided into natural and anthropogenic factors. Natural drivers of drought include changing weather patterns, altered air circulation, rising ocean temperatures, and reduced soil moisture. These processes result in increased evaporation, reduced rainfall, and climate change. Anthropogenic factors influencing drought include land-use practices such as using large amounts of water for crop irrigation, building large dams to generate electricity, and storing water in reservoirs, which influence downstream river flow, deforestation and mining [3].

It has been shown that, in recent years, widespread and frequent droughts have affected most of Europe, and the impact of anthropogenic factors on this phenomenon has also been examined. The analysis of the drought trend over the last 300 years was carried out using the annual record of oxygen isotopes in tree rings based on the CMIP6 model in Bosnia and Herzegovina. The reconstruction undertaken in this paper shows that the beginning of the drying trend in southern Europe dates back to around the 1850s. It is common knowledge that the risk of drought is closely related to global warming. However, the topic is rarely discussed in scientific publications, particularly when assessing drought-related losses [4].

In [5], it was indicated that the current drought trend may cause pronounced regional imbalances and affect many aspects of human life, due to a predicted temperature increase of 4°C by 2100. The greatest losses are expected in southern and western Europe, where drought may reduce regional agricultural economic output by 10%.

In [6], it was stated that long-term droughts have become a semi-permanent characteristic of the European climate, a trend that has been especially evident over the last 20 years. Long-term droughts in Europe are usually caused by anomalies in sea surface temperatures in the Pacific and Atlantic basins that persist for longer periods. The research used statistical methods (i.e. Canonical Correlation Analysis and Convergent Cross-Mapping) to assess the observed drying trend in central and southern Europe and its causes. After examining the spatiotemporal variability of annual drought in Europe using the SPEI12 model, the drought trend was linked to large-scale atmospheric and ocean anomalies. The long-term drought trend over southern and central Europe, captured by SPEI12, is linked to the centre of the Azores shifting towards Europe as a barotropic response to the SST structure south of Greenland. This is a response to the AMOC's long-term downward trend.

However, [7] reported extreme meteorological and hydrological droughts in large areas of northern Europe in 2018. They occurred because of large-scale atmospheric circulation. The study also examined the relationship between atmospheric circulation and streamflow in the Nordic region. The source of the drought, especially over Fennoscandia, was sea surface temperature anomalies exceeding 3°C in the Baltic Sea and Barents Sea. Moreover, groundwater levels were at record lows. The drought in the northern European region was found to be directly influenced by low streamflows in western/northern Norway driven by high-pressure systems over the Norwegian Sea. The rest of Scandinavia was influenced by low flows from the North Sea and a low-pressure system over Greenland and Russia at similar latitudes.

Drought monitoring and early warning (M&EW) systems have been developed for the UK, as described in [8]. These systems are a key element of drought preparedness. In M&EW systems, indicators such as the SPI (the Standardised Precipitation Index) are most often used. Meteorological and hydrological droughts were identified in the UK study area using the SPI and the associated Standard Stream Flow Index (SSFI). SPI and SSI time series were calculated for 121 basins, and their duration and severity, as well as the relationship between meteorological and hydrological drought, were examined by analysing the cross-correlation between 1-month SSI and different SPI accumulation periods. Research found that over short accumulation periods, meteorological drought is characterised by low spatial variability. However, hydrological droughts occurred less frequently, but when they did, they were longer and much more severe, especially in the south and east of the UK.

Many attempts have been made to address the problem of increasingly widespread drought, one such proposal being the Drought Information Satellite System (DISS). The model integrates meteorological data and satellite imagery. The aim of determining the index is to monitor the phenomenon under various conditions,

including meteorological and temperature conditions derived from MODIS, as well as environmental conditions. The DISS index showed that the central and western parts of Poland are the regions most strongly affected by drought, with cereal yields reduced by up to 30% [34].

The MODIS model has also been used to study several drought episodes in Central Europe since 2018. These events have had a strong impact on ecosystems and, by extension, on food production, and all indications are that they may intensify. In [35], EVI vegetation indices (from MODIS) based on satellite Earth observations were presented to characterise vegetation stress on arable land in Germany. They showed significant variation in drought patterns in recent years and large regional differences.

The numerous examples cited show that drought has been a problem throughout Europe for many years. This highlights the need for continued research, monitoring, assessment, and forecasting of drought, as well as for the development of effective mitigation strategies.

The most important role in drought assessment and prediction is played by hydrological and meteorological parameters, such as total water storage changes (TWS) and precipitation (P). The work uses these two parameters to derive climatic indices such as the Water Storage Deficit Index (WSDI) and the Combined Climatological Deviation Index (CCDI), calculated from data collected by the GRACE geodetic satellite mission and the MERRA-2 assimilation model. In the second step, forecasts of the examined indices were made for the next five years.

The work aims to assess the rate of drying in Europe and the extent of drought risk. The research attempts to test the hypothesis that the indices can serve as the basis for monitoring and predicting the course of drought. This is the first comprehensive analysis of the European water cycle and the long-term impact of climate change on declining water levels. Two components were selected that provide different information: high sensitivity to short-term anomalies (CCDI) and water shortages in the system over longer periods (WSDI), which together provide a comprehensive assessment. The study focused primarily on assessing and forecasting meteorological and hydrological drought using monthly values of total water storage and precipitation changes.

2. Materials and Methods

2.1. Case Study

The study was carried out across Europe, divided into climatic zones by the Köppen–Geiger classification, based on the analysis of average monthly temperatures and the amount and distribution of annual precipitation, as shown in Figure 1. The climate designation in the figure and the climate characteristics are consistent with Appendix 1.

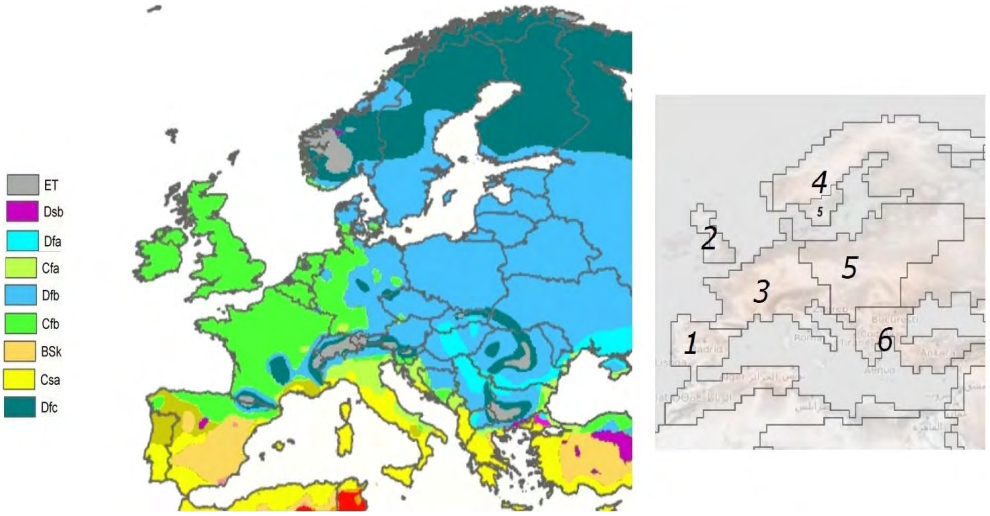

Fig. 1. Map of the study area: Europe divided
according to Köppen–Geiger climate classification and into research areas 1–6

2.2. Data

Two sets of time series were collected for each studied region: ΔTWS from the GRACE satellite mission and precipitation from the MERRA2 model.

Since the launch of the GRACE mission in 2002, satellite observations of TWS changes have provided a unique, global perspective on changes in terrestrial water resources. These changes are caused by both natural processes and human activity [9]. TWS is the total amount of stored water, i.e., water stored in reservoirs, groundwater, snow cover, soil moisture, rivers, lakes, glaciers, land ice, and biomass. Large fluctuations affect not only natural ecosystems but also human activity. TWS changes are caused by the loss of glacier mass or the flow or withdrawal of groundwater, and they respond to atmospheric and oceanic variability. TWS changes with the loss of balance among the main elements influencing its condition: precipitation (the dominant factor), evapotranspiration, and, to a lesser extent, surface runoff. For this reason, it is a key variable in the water budget [10]. Long-term TWS time series observations and models are fundamental to water resource analysis. These are fundamental to monitoring and predicting extreme meteorological phenomena such as droughts and floods, and for determining the effects of climate change [11].

Satellite remote sensing has enabled continuous monitoring of hydrological fluxes at various spatiotemporal resolutions [12]. One such mission is GRACE, which has been operating since March 2002 and provides quantitative estimates of long-term anomalies in total water storage [13, 14].

The monthly GRACE CSR TWSA RL06 product, with a global grid resolution of 1° (ca. 110 km), was obtained for this study. The user-friendly Level 3 product in

mascon form was considered without a scaling factor, and the analysis was based on raw mascons. The result was corrected for glacial isostatic adjustment (GIA) by subtracting the ICE-6G GIA model. No correction for land leakage was applied, and the analysis was based exclusively on grids covering land areas (Appendix 2). All grids extending into marine areas were excluded if they had no land fraction. No additional filtering was applied.

Precipitation formation over the land surface usually occurs through two mechanisms: advection of water vapour from the oceans and evaporation of surface moisture. In [15], it was estimated that, on average, 40% of precipitation comes from land evaporation, and 57% returns as precipitation over land. As a result of rising temperatures and climate change, rainfall distribution has changed spatially and temporally worldwide [16]. Long-term monitoring has produced exceptionally long precipitation time series. Traditionally, measurements were based on rain gauge records, which are point-based and allow observation of a small area of the studied region; additionally, such rain gauge measurements are not available everywhere. An alternative is the use of models derived from satellite observations, supplemented with in situ measurements, available worldwide on regular grids [17–19].

Modern-Era Retrospective Analysis for Research and Applications, version 2 (MERRA-2) is available via the Global Modelling and Assimilation Office (GMAO) of the National Aeronautics and Space Administration (NASA) and has been publishing data since 1980. It is the first model to include long-term reanalysis of satellite observations. A key characteristic of the model is that it captures the interactions with other physical processes in the climate system. MERRA-2 atmospheric variables are published with a spatial resolution of 0.5° × 0.625° [20].

For large, difficult-to-reach areas, satellite observations from the GRACE and GLDAS models are a unique source of data. However, this is not an ideal solution due to limited spatial resolution, and it cannot serve as an effective data source for local-scale applications. Precipitation uncertainties from MERRA-2 may propagate into CCDI calculations. The influence of anthropogenic water extraction cannot be isolated from GRACE TWS signals in this study. Region 4 is partially influenced by cryospheric processes, which can distort drought interpretation. The number of grids considered in the analysis is presented in Table 1.

Table 1. Grids included in the study for areas 1–6

Area number	Number of GRACE TWS grids	Number of MERRA grids	Number of full MERRA grids
1	54	153	119
2	26	81	57
3	155	443	380
4	302	440	378
5	223	650	562
6	49	147	101

Only full MERRA grids were considered. Both grids (GRACE TWS and MERRA) were harmonised using the area-weighted mean method (i.e., MERRA-2 data were regridded). The analysis was repeated with simple means; differences in CCDI/WSDI trends were less than 5%.

2.3. Methods

The paper presents an evaluation of drought in Europe using GRACE mission observations of total water storage changes supported by the MERRA-2 assimilation model. For this purpose, the CCDI and WSDI were computed. The transformation of data into indices is presented as a flowchart (Fig. 2).

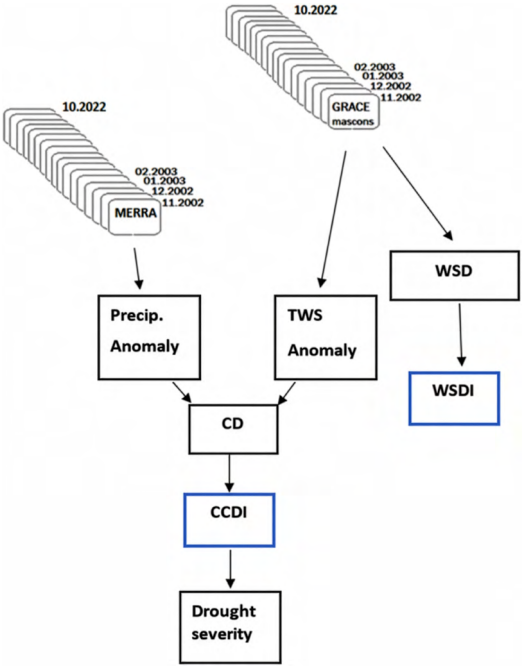

Fig. 2. Flowchart showing data flow and final indices computed in this paper

To carry out the study, GRACE (in netCDF format from https://grace.jpl.nasa.gov/data/get-data/jpl_global_mascons/ as mascon grids) and precipitation time series observations from the MERRA model (in ASCII format from https://giovanni.gsfc.nasa.gov/giovanni/) were acquired, covering only land, for the period from November 2002 to October 2022. The units were standardised: MERRA water-storage values were converted to centimetres using the relation 1 kg/m² = 1 mm of water-column height, and the flux values (kg/m²/s) were converted to cumulative monthly values by multiplying them by the number of seconds in each month. The models have different resolutions (GRACE 1° × 1° over the mascon area, and MERRA 0.5° × 0.625°),

which is also a significant limitation in the research, as it is often insufficient. However, the goal of the study was to assess entire large climatic areas of Europe, over which each model's grid is averaged (arithmetic mean), so there was no need to standardise these grids. The prepared time series at a monthly resolution was then used to calculate and assess climate changes in each designated area. The observations were used along two paths, as shown in the flowchart (CCDI and WSDI).

The CCDI quantifies the relationship between atmospheric and terrestrial water. The index determines the occurrence of meteorological, hydrological, agricultural, and anthropogenic droughts [21, 22]. The CCDI is the sum of monthly observations of total water storage anomalies (TWSA) and monthly precipitation anomalies (PA) [21]:

$$PA = P - \overline{P} \text{ [cm]} \tag{1}$$

where: PA – precipitation anomaly time series, P – precipitation time series, $\overline{P}$ – monthly average precipitation value.

Residuals are computed [21]:

$$PA^R = PA - \overline{PA} \text{ [cm]} \tag{2}$$

where: PA^R – precipitation anomaly residual time series, $\overline{PA}$ – average precipitation anomaly for a given month.

Total water storage anomaly residuals from the GRACE observations are [21]:

$$TWSA^R = TWSA - \overline{TWSA} \text{ [cm]} \tag{3}$$

where: $TWSA^R$ – total water storage anomaly residual time series, $TWSA$ – total water storage anomaly time series, $\overline{TWSA}$ – monthly average total water storage anomaly value.

So, climatological deviation (CD) is [21]:

$$CD = PA^R + TWSA^R \text{ [cm]} \tag{4}$$

and Combined Climatological Deviation Index (CCDI) is [21]:

$$CCDI = \frac{\left(CD - \overline{CD}\right)}{st.dev.(CD)} \tag{5}$$

where: CD – combined precipitation and total water storage anomaly deviation, $\overline{CD}$ – monthly average value of CD, $st.dev.(CD)$ – standard deviation of CD.

Once the CCDI has been computed, drought severity can be assessed [21]. Its values are presented in Appendix 3. The Drought Severity Index (DSI) is classified for each time step based on the computed CCDI values.

Water storage deficit is the difference between the total water storage anomaly and the average monthly total water storage anomaly [21]:

$$WSD = TWSA - \overline{TWSA} \tag{6}$$

where: WSD – water storage deficit, $TWSA$ – total water storage anomaly time series, $\overline{TWSA}$ – long-term mean value of total water storage anomaly.

Water Storage Deficit Index is given by [23]:

$$WSDI = \frac{WSD - \overline{WSD}}{st.dev(WSD)} \tag{7}$$

where: $WSDI$ – water storage deficit index time series, WSD – water storage deficit, $\overline{WSD}$ – mean value of the water storage deficit, $st.dev.(WSD)$ – standard deviation of the water storage deficit.

CCDI and WSDI forecasts were produced using the AutoRegressive Integrated Moving Average (ARIMA) method, previously used and described in [24]. This method can be used only when observations are characterised by trend and seasonality. The ARIMA(p,d,q) model aims to find optimal values of p, d and q. To ensure full transparency of the forecasting procedure, a complete statistical diagnostic workflow was applied. Stationarity of each regional CCDI and WSDI series was assessed using both the Augmented Dickey–Fuller (ADF) and KPSS tests. ADF was used to detect unit roots, while KPSS was used to test for trend stationarity, ensuring a consistent interpretation. For all regions, seasonal components with a 12-month period were tested; where relevant, SARIMA models were fitted in parallel. Autocorrelation and partial autocorrelation functions (ACF/PACF) were analysed to identify autoregressive (p) and moving-average (q) orders. Several ARIMA(p,d,q) and SARIMA(P,D,Q) candidate models were then estimated. Forecasts were generated with 95% confidence intervals, and all error metrics (MAE – mean absolute error, RMSE – root mean square error, and MASE – mean absolute scaled error) were computed relative to the naïve seasonal benchmark.

The determined errors are based on squared errors. If we assume that Y_t denotes an observation at time t, then for a given forecast we can define the forecast error as $e_t = Y_t - F_t$, where F_t is the forecast. Given that MSE is defined as e_t^2, we can then compute [25]:

$$RMSE = \sqrt{MSE} \tag{8}$$

and:

$$MAE = mean\left(\left|e_t\right|\right) \tag{9}$$

Error scaling based on MAE gives a scaled error defined as [26]:

$$q_t = \frac{e_t}{\frac{1}{n-1}\sum_{i=2}^{n}\left|Y_i - Y_{i-1}\right|} \tag{10}$$

Finally, MASE is [35]:

$$MASE = mean\left(\left|q_t\right|\right) \tag{11}$$

3. Results

3.1. Analysis of ΔTWS and Precipitation Changes

First, TWS and precipitation changes were determined for each area (Appendix 4 – Fig. A4). For areas 1, 3, 4, and 5, ΔTWS decreased significantly after the start of the GRACE-FO mission. For areas 1 and 2, the lowest ΔTWS amplitudes were found (between −5 and 5 cm). These areas are located in the westernmost part of Europe and are most strongly influenced by the oceanic climate. By contrast, the highest amplitudes were recorded in eastern Europe (areas 5 and 6; between −15 and 15 cm), i.e., in regions most strongly influenced by the Asian continent. In all areas, maximum values were observed in the autumn months, and minimum ΔTWS values were observed in the spring months.

It is evident that changes in precipitation are many times smaller than the ΔTWS time series. It was determined that the ΔTWS response to precipitation change in area 1 exhibits a 3-month lag (Fig. A4a), with values ranging from 0 to 0.5 cm. Area 2 is characterised by high rainfall irregularity (Fig. A4b) and no constant periodic factor, and no consistent lag was observed. In area 3, there are years with small amplitudes throughout the year (2005–2007, 2009), whereas in 2010, there is no consistent seasonal pattern as in the other periods studied; in that year, regular increases and decreases in the amplitude of precipitation changes were observed. The lag relative to ΔTWS is 1–3 months. Amplitudes ranged from 0.2 to 0.4 cm (Fig. A4c). In area 4, very small and regular amplitudes were observed (0.3–0.4 cm), and precipitation changes were in antiphase with TWS changes: periods of maximum TWS corresponded to periods of minimum precipitation change, and vice versa. This was probably strongly influenced by the fact that area 4 largely overlaps with the Arctic, which has a harsh and dry climate (Fig. A4d). In area 5, with very stable and insignificant amplitudes (values of approximately 0.3 cm of precipitation changes), no significant lag in precipitation changes relative to TWS changes was observed (Fig. A4e). Area 6 includes rainfall changes of 0.2–0.6 cm. High regularity and seasonality of changes were observed, with a 4–5-month lag relative to ΔTWS (Fig. A4f).

3.2. Determination of the Combined Climatological Deviation Index

After a preliminary analysis of the basic components required for further calculations in the research, the time series of the CCDI was determined (Fig. 3). No uniform or constant phases were observed across all study areas; instead, the minimum and maximum values occurred in completely different periods of the year.

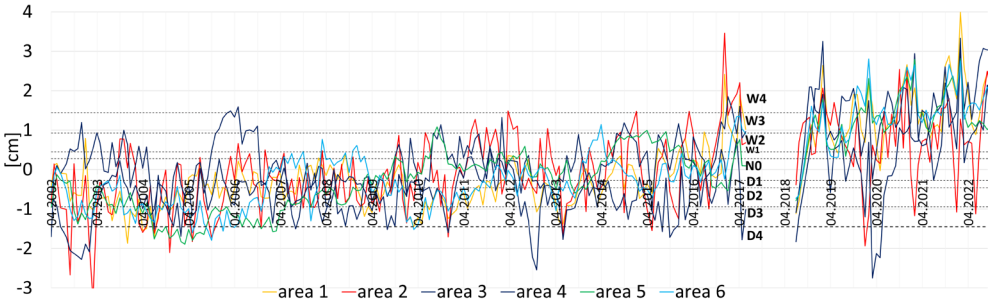

Fig. 3. Combined Climatological Deviation Index for areas 1–6

In area 1, higher amplitudes and more frequent 'wet' conditions were observed from 2016. In earlier periods, N0 was rarely exceeded; most values ranged between D3 and D1. In general, CCDI reached maximum values in winter and minimum values in summer.

In area 2, it was noted that until 2005, CCDI values dropped to zone D4 in spring; until 2016, they fluctuated between D3 and W2, and then until 2020, they remained exclusively within the 'wet' range. In the winter of 2020, another decline in D4 was recorded. At the turn of 2015/2016, a marked rise in CCDI was noticed in the W4 zone (approximately 3.5 cm).

Area 3 has an irregular CCDI series. At the beginning of the study, in 2002 and 2003, all values were in the 'dry' range, even reaching D4 values in winter. From 2004 to 2016, regular and seasonal fluctuations between D2 and W1 were observed, with minima in spring and autumn and maxima in summer and winter. At the end of the study period, values are in the 'wet' range, reaching even W4 in autumn.

The largest deviations were observed for area 4, especially in the years 2006, 2012, and 2022. Only in the period 2006–2009 were smaller amplitudes observed, ranging from D3 to D1. In the periods 2002–2004, 2010–2012, and 2013–2015, the values fluctuated exclusively in the wet range.

Area 5 in the years 2002–2009 had values within the 'dry' range, even with a decrease to D4 in 2004 and 2005. The second part of the study period includes only 'wet' values, ranging from N0 to W3 and reaching W4 in the winter of 2018 and 2019. No regular seasonal pattern could be identified.

Area 6 is very variable. From 2002 to 2006, values in the 'dry' range (D2–D3) were observed; from 2007 to 2009, there were 'wet' values (N0–W2), except for winter 2007, when a drop to D3 was observed. The period 2009–2013 was 'dry' (N0–D3).

From 2013 to the end of the study period, 'wet' range values rose steadily, with increasing amplitudes and reaching up to D4 in the winter of 2019/2020. Maximum CCDI values occurred regularly in autumn.

CCDI reveals high interannual variability. Several regions exhibit a clear shift towards wetter anomalies before 2016, followed by sustained drying trends after 2018. Maximum positive CCDI values often occur in winter, whereas minimum values show greater seasonal variability.

3.3. Determination of the Water Storage Deficit Index

The second parameter used to determine drought severity in this study was WSDI (Fig. 4). Regular seasonality is evident across all studied areas: maximum values occur in the spring months (wet months), while minimum values occur in the autumn months (dry months). The greatest differences were found in area 2. In this area, compared to the others, there are no sinusoidal increases or decreases in the WSDI value; instead, month-to-month jumps were observed. Area 1 is in the D1 to W3 range until the end of 2015, then falls to the N0–D2 range. Much higher WSDI amplitudes were observed in area 2, regularly in the D1–W3 range with single peaks to W4 in the winter of 2003 and 2020 and to D3 in the winter of 2016. Area 3 showed a regular sinusoidal pattern, with values ranging from D1 to W2 during the period 2002–2017 and from N0 to D2 during the period 2018–2022. Area 4 reaches values of W2 every spring and D2 every fall, except in the spring of 2020, when WSDI reached W4. Area 5 is characterised by 'wet' values in the N0–W3 range from 2002–2009, then declines to reach lower values until the end of the study period, in the N0–D2 range. For area 6, during the GRACE mission period, WSDI ranged between D1 to W2, except in 2007 and 2008, when the maximum value reached W1, and in 2014 and 2017, when it reached N0. In 2018–2022, the amplitudes were constant, but a regular decrease in values towards D2/D3 was noticeable.

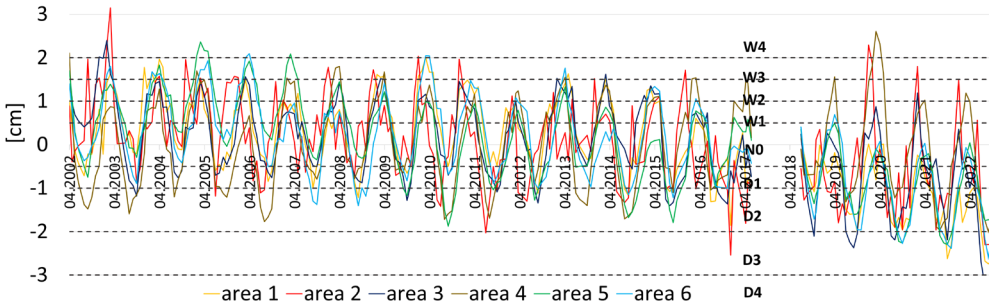

Fig. 4. Water Storage Deficit Index for areas 1–6

WSDI demonstrated more regular behaviour than CCDI, displaying consistent seasonal cycles. Notably, the frequency and magnitude of negative WSDI values (indicating dry conditions) increased significantly after 2018 in most regions.

3.4. CCDI and WSDI Prediction with Bias Evaluation

The last study conducted was a forecast of CCDI and WSDI values for the next 5 years, with an assessment of the forecast (Appendix 5). Additionally, the trends of CCDI and WSDI changes were determined. An always-positive CCDI trend and an always-negative WSDI trend were found. To determine the trend, the forecast trajectory of the time series was also considered.

To predict future time-series patterns, the time series was normalised (seasonality, random noise, and trend were identified), enabling ARIMA forecasting. The best ARIMA model was selected based on the specified parameters, with p, d, and q kept as small as possible. For the data presented in the manuscript, the selected values were $p = 2$, $d = 0$, and $q = 2$, corresponding to an ARIMA(2,0,2) model. The forecast was based on the full time series (November 2002 to October 2022). The ARIMA forecast suggests that the WSDI is more predictable than the CCDI.

A 95% confidence level was set for all forecasts, and fluctuation bands were prepared. In most CCDI forecasts, the confidence bands gradually widened, indicating relatively good confidence in the future dynamics of the CCDI. However, the analysis also showed that the greater the variability of the time series (e.g., area 4), the wider the bands. Overall, the CCDI forecasts are relatively stable. In the case of the WSDI, the forecasts show significantly wider fluctuation bands than CCDI forecasts. In series with strong seasonality (e.g., area 3, area 4, area 6), the bands take on a wavy shape, suggesting a greater amplitude of future changes. The analysis showed that the WSDI forecasts are subject to significantly greater uncertainty, resulting from stronger seasonality and frequent downward trends.

Based on Table 2, the strongest increasing trend in the CCDI time series was observed in area 5 (0.0111 cm/year). Similarly, the most negative WSDI trend was found in area 5 (−0.0084 cm/year).

Table 2. Trend values and R^2 values for CCDI and WSDI for areas 1–6

Area number	CCDI		WSDI	
	Trend value [cm/year]	R^2 value	Trend value [cm/year]	R^2 value
1	0.0096	0.4794	−0.0081	0.3500
2	0.0073	0.2807	−0.0066	0.2241
3	0.0096	0.4786	−0.0067	0.2391
4	0.0019	0.0176	−0.0003	0.0006
5	0.0111	0.6496	−0.0084	0.3736
6	0.0105	0.5782	−0.0073	0.2793

Area 4 showed the smallest positive CCDI trend (0.0019 cm/year). For this area, the WSDI trend was small (−0.0003 cm/year). To determine the proportion of variance explained by the regression model, the coefficient of determination (R^2) was calculated for the time series (Table 2). The highest values were observed in areas 5 and 6 for CCDI (0.6496 and 0.5782, respectively). The R^2 values for CCDI were also markedly higher than those for WSDI. The lowest values were found for area 3, namely 0.0176 and 0.0006 for CCDI and WSDI, respectively.

The widely used Mann–Kendall (MK) test was performed for the time series. This non-parametric statistical test is used to determine whether a time series exhibits a monotonic increasing trend, a monotonic decreasing trend, or no trend at all when the changes are random. The MK test does not assume linearity of the trend, only its direction. For each area, the S statistic was determined for CCDI and WSDI, then standardised to Z to determine the significance level p (Table 3).

Table 3. Mann–Kendall test, and Sen's slope values for CCDI and WSDI for areas 1–6

Area number	CCDI		WSDI	
	Mann–Kendall test	Sen's slope [cm/month]	Mann–Kendall test	Sen's slope [cm/month]
1	S = 15,175 Z = 11.482 p = 0.0000	0.0082	S = −4,409 Z = −3.341 p = 0.0008	−0.0028
2	S = 10,965 Z = 8.296 p = 0.0000	0.00667	S = −10,643 Z = −8.086 p = 0.0000	−0.0067
3	S = 14,583 Z = 11.034 p = 0.0000	0.0081	S = −8,908 Z = −6.739 p = 1.58e−11	−0.0057
4	S = 4,063 Z = 3.073 p = 0.0021	0.0026	S = −180 Z = −0.135 p = 0.8923	−0.0001
5	S = 481.0 Z = 0.363 p = 0.7160	0.0003	S = −12,864 Z = −9.733 p = 0.0000	−0.0079
6	S = 3,802 Z = 2.877 p = 0.0040	0.0024	S = −1,0416 Z = −7.881 p = 3.1e−15	−0.0066

As a supplement to the MK test, Sen's slope (also known as the Theil–Sen estimator) was calculated. This is a non-parametric estimator of trend that expresses the average change in a time series value per unit of time. For each point in the

series, the slopes between all pairs of points were calculated. The analysis showed a strongly increasing trend for CCDI in areas 1, 2, 3, 4 and 6 (significant increasing trends). No significant trend was observed for CCDI for area 5 and WSDI for area 4 (insignificant trend). For WSDI in areas 1, 2, 3, 5, and 6, a strongly decreasing trend was observed (significant decreasing trends). A positive Sen's slope indicates that the index increases over time (e.g. mass accumulation, increase in humidity, increase in resources), while a negative Sen slope indicates a decline (e.g. drying or decrease in resources). The strongest upward trends in CCDI were found in areas 1 and 3, and the strongest downward trends for WSDI were found in areas 2 and 5.

To assess the predictive model's accuracy, three statistical measures were used: MASE, MAE, and RMSE (Table 4). MAE was calculated as the average absolute difference between the model's fitted values and the observed historical data. MASE was defined as the ratio of the model MAE to the MAE of a naïve model that predicts the value at time point t from the previous observation. RMSE can be interpreted as the average expected difference between the predicted and observed values.

Table 4. Statistics for the forecasts for areas 1–6

Area number	CCDI			WSDI		
	MASE	MAE [cm]	RMSE [cm]	MASE	MAE [cm]	RMSE [cm]
1	1.70	0.57	0.75	0.95	0.38	0.46
2	1.11	0.80	1.00	1.27	0.79	0.96
3	2.59	0.82	0.96	1.29	0.48	0.57
4	1.39	0.73	1.05	0.74	0.32	0.41
5	2.92	0.54	0.71	0.67	0.22	0.30
6	1.16	0.34	0.47	0.64	0.23	0.30

The analysis of the predictions using MAE showed that the smallest range of deviations in the forecast values was found for area 6 (0.34 cm) for CCDI and area 5 and area 6 (0.22 cm and 0.23 cm, respectively) for WSDI. MAE for WSDI are generally much lower than those for CCDI. Across all MASE values for the CCDI time-series prediction, the selected model performed worse than the naïve model (values of 1.11–2.92, with the worst values in area 5 and the best in area 2). The WSDI model forecast for areas 1, 4, 5, and 6 outperformed the naïve model, with the highest accuracy for area 6 (0.64). For areas 2 and 3, the naïve WSDI model performed better than the model's forecast (1.27 and 1.29, respectively). RMSE values were approximately twice as high for CCDI as for WSDI (except area 6, where they were similarly low, and area 2, where they were similarly high).

WSDI has much lower MAE and RMSE, and the MASE value shows that the ARIMA model is practically useful in most regions. Therefore, it can be concluded that water deficit is a more stable and predictable process than cumulative atmospheric and hydrological anomalies. CCDI is characterised by greater variability, which results from seasonal variations in precipitation and short-term extreme events.

The high MASE values are noteworthy. Values above 1 indicate that the CCDI and WSDI time series have a strong random component, episodic variability, and a complex seasonal structure, which prevents forecasting models from reproducing their behaviour better than simple forecasting. This is typical of hydrological and climatological indices, which respond non-linearly to meteorological variables and extreme events. A high MASE indicates that the variability of the analysed index is difficult to predict using statistical methods. One possible approach would be to remove seasonality from the time series or to denoise the data by calculating a moving average. Future research could employ a better model (e.g., SARIMA).

Because MASE exceeded 1 for several regions, the ARIMA forecasts do not outperform a naïve seasonal persistence model. Consequently, the long-term projections should be interpreted cautiously. Trend estimates (Mann–Kendall test and Sen's slope) are therefore reported separately from the ARIMA forecasts to avoid conflating structural tendencies with short-term predictability. Uncertainty bands are reported using 95% confidence intervals. When the interval width exceeds the absolute value of the forecast anomaly, the prediction is considered statistically inconclusive. In addition to ARIMA, alternative models were considered, including SARIMA and ARIMAX with precipitation as an exogenous variable. Error metrics were compared to verify whether seasonality or external forcing improved model skill.

All CCDI and WSDI time series exhibited non-stationarity, as indicated by the ADF test ($p > 0.05$ for all regions) and confirmed by the KPSS test ($p < 0.05$). This required first-order differencing, and seasonal differencing (lag 12) was necessary to remove the annual cycle.

Comparison of ARIMA(2,0,2) and SARIMA(0,1,1)(0,1,1) models based on AIC and BIC values showed consistent improvement when seasonal structure was included (Appendix 6). Across all regions, SARIMA reduced AIC by 8–12% relative to ARIMA, indicating a substantially better fit. Residual diagnostics confirmed the absence of significant autocorrelation (Ljung–Box $p > 0.10$) and showed approximate normality of residuals. These results demonstrate that SARIMA provides an appropriate statistical representation of the monthly dynamics of both CCDI and WSDI.

Forecast skill varied by region. Because MASE exceeded 1 in several cases, forecasts were interpreted cautiously and used only as an illustrative extension of historical trends. SARIMA consistently outperformed ARIMA, confirming the importance of capturing monthly seasonality in hydrological indices.

3.5. Model Validation

The Pearson correlation coefficient r measures the strength and direction of the linear relationship between two variables and ranges from −1 to +1. For hydrological drought indices, correlations are typically:

– r = 0.5–0.8 for indices like TWSA (such as CCDI),
– r = 0.3–0.6 for water-climate indices (such as WSDI),

where higher correlations are generally observed for SPEI-12 than for SPEI-3. For model validation, SPEI and soil-moisture data from GLDAS were used.

CCDI shows consistently strong correlations with SPEI-12 across all regions (r = 0.58–0.74), confirming that CCDI successfully captures long-term hydroclimatic anomalies (Table 5). WSDI correlates moderately with SPEI-3 (r = 0.35–0.51), reflecting its sensitivity to short-term wet-dry anomalies (Table 6). CCDI matches well with GLDAS soil moisture anomalies, supporting the physical interpretation of CCDI as a groundwater-soil moisture composite signal (Table 7).

Table 5. Correlation between CCDI and SPEI-12

Area number	Correlation	p-value
1	0.71	<0.001
2	0.66	<0.001
3	0.63	<0.001
4	0.58	<0.001
5	0.74	<0.001
6	0.69	<0.001

Table 6. Correlation between WSDI and SPEI-3

Area number	Correlation	p-value
1	0.42	<0.01
2	0.38	<0.01
3	0.47	<0.01
4	0.35	<0.01
5	0.51	<0.01
6	0.41	<0.01

Table 7. Correlation between TWSA and soil moisture from GLDAS

Area number	Correlation
1	0.68
2	0.59
3	0.64
4	0.55
5	0.73
6	0.61

To assess the reliability of CCDI and WSDI, the indices were compared with two independent benchmarks: the Standardised Precipitation Evapotranspiration Index (SPEI) and GLDAS soil moisture anomalies. CCDI showed strong and statistically significant correlations with SPEI-12 (r = 0.58–0.74), indicating high sensitivity to long-term hydroclimatic conditions. WSDI correlated moderately with SPEI-3 (r = 0.35–0.51), reflecting its shorter-term response characteristics. Additionally, CCDI correlated well with GLDAS soil moisture (r = 0.55–0.73), confirming that the index captures relevant hydrological variability.

These results collectively demonstrate that CCDI and WSDI provide credible and physically meaningful information on drought and wetness anomalies.

4. Discussion

Monitoring and predicting droughts are essential for sustainable water management. The paper aims to assess the extent and progression of drought in Europe using the CCDI and the WSDI.

For Europe, the Combined Drought Index (CDI) is used by the EDO [27]. Based on 10 years of research, drought has been observed to be a cascading process. This is evident in how a rainfall deficit translates into a soil water deficit. This observation is important given the shift in the drought risk management paradigm. The current approach has shifted from a reactive approach to a proactive approach [28]. For early warning, it is extremely important to monitor climate trends, as the analysis showed that major drought events occurred in central Europe in 2003, in the Iberian Peninsula in 2005, and in northern Europe in 2018. Based on the research presented in this paper, it can be concluded that a drought period in Europe has lasted since 2018. In 2003, it was confirmed that the drought occurred mainly in central Europe. In 2005 and 2006, a period of significant drought was observed in the Iberian and Balkan Peninsulas (areas 1 and 4). According to [29], an increasing divergence in the groundwater deficit index across Europe has been observed. The

study showed regional discrepancies in the probability of meteorological drought based on observations of evapotranspiration and precipitation in Europe. It was noticed that differences in temperature increases had a major impact, especially in the years 1970–2014, significantly affecting evapotranspiration. An increasing frequency of drought periods in southern Europe and a decrease in northern Europe were indicated. This observation is consistent with climate change projections. The research presented in [30–32] also confirmed that southern Europe is the hottest region on the continent and is experiencing drought-related climate changes. There is a clear reversal in polarity in the north-south comparison [32, 33]. The same observations are based on the research presented here. The CDI is often used for early warning of droughts. One of its implementations is the EDO, which focuses on identifying actual and potential damage to vegetation by showing the progression of rainfall deficits in the hydrological cycle. However, the model suffers from questionable observation reliability, particularly due to its spatial resolution and the specific use of FPAR or SPEI algorithms [36, 37].

5. Conclusions

Based on the research,, the following conclusions were drawn:

- Because the study was conducted in areas with different climatic conditions, the method may also be applicable to other regions.
- ΔTWS is characterised by much greater seasonality than precipitation; maximum ΔTWS values were observed in each studied area, and the minimum values were observed in autumn. Areas located in the westernmost part of Europe, most influenced by the oceanic climate, are characterised by the lowest ΔTWS amplitudes (between −5 and 5 cm). The highest amplitudes were observed in eastern Europe, with the greatest influence of the Asian continent (from −15 to 15 cm). In some areas, a lag between precipitation changes and ΔTWS can be determined (areas 1, 3, and 6).
- There are no regular phases in the case of the CCDI index; minimum and maximum values occur in completely different periods of the year. In many research areas, time series do not exhibit regularity. Generally, areas 1, 2, 3, 5, and 6 are characterised by a noticeable threat of climate drying, especially since 2018.
- Unlike CCDI, WSDI shows high regularity and seasonality. There is also a noticeable increase in the wet zone deficit. The least regular area turned out to be area 2, where there are no regular increases and decreases in the WSDI value (because of the largest amount of precipitation during the year, a mild climate, the lowest intra-annual variability due to the proximity of the ocean, and small fluctuations in annual evapotranspiration and ice melting). Since 2018, periods of 'wet' and 'dry' deficits in the total water storage record across the studied areas have been increasingly frequent.

- Trend analysis indicates that, for almost all areas, there is a tendency towards drying, and both downward and upward shifts are evident. Area 4, covering Scandinavia, appears to be the most stable. However, this area includes Arctic areas covered with ice. Melting ice supplies water to the system, distorting the overall picture. This area should be divided into smaller subregions and analysed in more detail. Area 6 appears to have the greatest risk of drought, due to the most rapid changes.
- The forecast indicates that the current state and rate of drought will continue.
- The predictive analysis shows that the prediction is more accurate in the case of the WSDI model. MAE for WSDI are much smaller than those for CCDI. For all MASE values of the CCDI time series prediction, the selected model is worse than the naïve model; by contrast, the WSDI model forecast shows that the created forecast model is better than the naïve model (except for areas 2 and 3). RMSE values are approximately twice as high for CCDI as for WSDI (except for area 6, where they are similarly low, and area 2, where they are similarly high).
- The CCDI and the WSDI are very useful in studies of drought in Europe.
- CCDI strongly reflects the combined meteorological and hydrological influence and shows high sensitivity to short-term anomalies, while WSDI reflects water shortages in the system more stably, and its seasonality is more pronounced.
- The use of these indices to determine drought risk is extremely useful, especially in spatial planning and water management (planning land improvement or retention reservoirs), investment planning, or even afforestation strategies.

Identifying effective drought mitigation strategies is essential, especially for ensuring agricultural productivity. Identifying areas at risk and potential changes within them using indices supports decision-making by assessing regional environmental conditions and identifying areas requiring urgent intervention [37]. Most often, drought monitoring indices serve as warnings that prompt the preparatory stage, for example, in the form of notifications to farmers [38]. Combining CCDI and WSDI allows local decision-makers to develop irrigation schedules, implement water-use restrictions, or implement water withdrawal restrictions.

Funding

This research received no specific grant from any funding agency in the public, commercial, or not-for-profit sectors.

Declaration of Competing Interests

The author declares that she has no known competing financial interests or personal relationships that could have appeared to influence the work reported in this paper.

Data Availability

Data will be available on request.

Use of Generative AI and AI-Assisted Technologies

No generative AI or AI-assisted technologies were employed in the preparation of this manuscript.

References

[1] Dregne H., Kassas M., Rozanov B.: *A new assessment of the world status of desertification*. Desertification Control Bulletin, no. 20, 1991, pp. 6–18.

[2] Sterk G., Stoorvogel J.J.: *Desertification–scientific versus political realities*. Land, vol. 9(5), 2020, 156. https://doi.org/10.3390/land9050156.

[3] Nandgude N., Singh T.P., Nandgude S., Tiwari S.: *Drought prediction: A comprehensive review of different drought prediction models and adopted technologies*. Sustainability, vol. 15(15), 2023, 11684. https://doi.org/10.3390/su151511684.

[4] An W., Xu C., Marković S.B., Sun S., Sun Y., Gavrilov M.B., Govedar Z., Hao Q., Guo Z.: *Anthropogenic warming has exacerbated droughts in southern Europe since the 1850s*. Communications Earth & Environment, vol. 4, 2023, 232. https://doi.org/10.1038/s43247-023-00907-1.

[5] Naumann G., Cammalleri C., Mentaschi L., Feyen L.: *Increased economic drought impacts in Europe with anthropogenic warming*. Nature Climate Change, vol. 11, 2021, pp. 485–491. https://doi.org/10.1038/s41558-021-01044-3.

[6] Ionita M., Nagavciuc V., Scholz P., Dima M.: *Long-term drought intensification over Europe driven by the weakening trend of the Atlantic Meridional Overturning Circulation*. Journal of Hydrology: Regional Studies, vol. 42, 2022, 101176. https://doi.org/10.1016/j.ejrh.2022.101176.

[7] Bakke S.J., Ionita M., Tallaksen L.M.: *The 2018 northern European hydrological drought and its drivers in a historical perspective*. Hydrology and Earth System Sciences, vol. 24(11), 2020, pp. 5621–5653. https://doi.org/10.5194/hess-24-5621-2020.

[8] Barker L.J., Hannaford J., Chiverton A., Svensson C.: *From meteorological to hydrological drought using standardised indicators*. Hydrology and Earth System Sciences, vol. 20(6), 2016, pp. 2483–2505. https://doi.org/10.5194/hess-20-2483-2016.

[9] Hirschi M., Seneviratne S.I.: *Basin-scale water-balance dataset (BSWB): An update*. Earth System Science Data, vol. 9(1), 2017, pp. 251–258. https://doi.org/10.5194/essd-9-251-2017.

[10] Humphrey V., Rodell M., Eicker A.: *Using satellite-based terrestrial water storage data: A review*. Surveys in Geophysics, vol. 44(5), 2023, pp. 1489–1517. https://doi.org/10.1007/s10712-022-09754-9.

[11] Yu Q., Wang S., He H., Yang K., Ma L., Li J.: *Reconstructing GRACE-like TWS anomalies for the Canadian landmass using deep learning and land surface model*. International Journal of Applied Earth Observations and Geoinformation, vol. 102, 2021, 102404. https://doi.org/10.1016/j.jag.2021.102404.

[12] Becker M., Papa F., Frappart F., Alsdorf D., Calmant S., Da Silva J.S., Prigent C., Seyler F.: *Satellite-based estimates of surface water dynamics in the Congo River Basin*. International Journal of Applied Earth Observations and Geoinformation, vol. 66, 2018, pp. 196–209. https://doi.org/10.1016/j.jag.2017.11.015.

[13] Heimhuber V., Tulbure M.G., Broich M., Xie Z., Hurriyet M.: *The role of GRACE total water storage anomalies, streamflow and rainfall in stream salinity trends across Australia's Murray-Darling Basin during and post the Millennium Drought*. International Journal of Applied Earth Observations and Geoinformation, vol. 83, 2019, 101927. https://doi.org/10.1016/j.jag.2019.101927.

[14] Rzepecka Z., Birylo M., Jerker J., Feifei C., Pietroń J.: *Groundwater storage variations across climate zones from southern Poland to Arctic Sweden: Comparing GRACE-GLDAS models with well data*. Remote Sensing, vol. 16(12), 2024, 2104. https://doi.org/10.3390/rs16122104.

[15] van der Ent R.J.: *A New View on the Hydrological Cycle over Continents*. Delft University of Technology, Delft, The Netherlands 2014 [Ph.D. thesis]. https://doi.org/10.4233/uuid:0ab824ee-6956-4cc3-b530-3245ab4f32be.

[16] Fallah A., Sungmin O., Orth R.: *Climate-dependent propagation of precipitation uncertainty into the water cycle*. Hydrology and Earth System Sciences, vol. 24(7), 2020, pp. 3725–3735. https://doi.org/10.5194/hess-24-3725-2020.

[17] Birylo M., Rzepecka Z., Nastula J.: *Assessment of the water budget from GLDAS model*, [in:] *2018 Baltic Geodetic Congress: BGC-Geomatics 2018: Proceedings: 21–23 June 2018, Olsztyn, Poland*, IEEE, 2018, pp. 86–90. https://doi.org/10.1109/BGC-Geomatics.2018.00022.

[18] Medrano S.C., Satgé F., Molina-Carpio J., Zolá R.P., Bonnet M.P.: *Downscaling daily satellite-based precipitation estimates using MODIS cloud optical and microphysical properties in machine-learning models*. Atmosphere, vol. 14(9), 2023, 1349. https://doi.org/10.3390/atmos14091349.

[19] Lei H., Zhao H., Ao T.: *A two-step merging strategy for incorporating multi-source precipitation products and gauge observations using machine learning classification and regression over China*. Hydrology and Earth System Sciences, vol. 26(11), 2022, pp. 2969–2995. https://doi.org/10.5194/hess-26-2969-2022.

[20] Baba M.W., Boudhar A., Gascoin S., Hanich L., Marchane A., Chehbouni A.: *Assessment of MERRA-2 and ERA5 to model the snow water equivalent in the High Atlas (1981–2019)*. Water, vol. 13(7), 2021, 890. https://doi.org/10.3390/w13070890.

[21] Sinha D., Sayed T.H., Reager J.T.: *Utilizing combined deviations of precipitation and GRACE-based terrestrial water storage as a metric for drought characterization: a case study over major Indian river basins*. Journal of Hydrology, vol. 572, 2019, pp. 294–307. https://doi.org/10.1016/j.jhydrol.2019.02.053.

[22] Birylo M., Rzepecka Z.: *Remote sensing-based hydro-extremes assessment techniques for small area case study (the case study of Poland)*. Remote Sensing, vol. 15(21), 2023, 5226. https://doi.org/10.3390/rs15215226.
[23] Thomas B.F., Reager J.T., Famiglietti J.S., Rodell M.: *A GRACE-based water storage deficit approach for hydrological drought characterization*. Geophysical Research Letters, vol. 41(5), 2014, pp. 1537–1545. https://doi.org/10.1002/2014GL059323.
[24] Birylo M., Rzepecka Z., Kuczynska-Siehien J., Nastula J.: *Analysis of water budget prediction accuracy using ARIMA models*. Water Science & Technology: Water Supply, vol. 18(3), 2017, pp. 819–830. https://doi.org/10.2166/ws.2017.156.
[25] Chase Ch.: *Demand-Driven Forecasting: A Structured Approach to Forecasting* (2nd ed.). Wiley, 2013.
[26] Hyndman R.J., Koehler A.B.: *Another look at measures of forecast accuracy*. International Journal of Forecasting, vol. 22(4), 2006, pp. 679–688. https://doi.org/10.1016/j.ijforecast.2006.03.001.
[27] Cammalleri C., Arias-Muñoz C., Barbosa P., de Jager A., Magni D., Masante D., Mazzeschi M., McCormick N., Naumann N.G., Spinoni J., Vogt J.: *A revision of the Combined Drought Indicator (CDI) used in the European Drought Observatory (EDO)*. Natural Hazards and Earth System Sciences, vol. 21(2), 2021, pp. 481–495. https://doi.org/10.5194/nhess-21-481-2021.
[28] Wilhite D.A., Pulwarty R.S.: *Drought and water crises: Lessons learned and the road ahead*, [in:] Wilhite D.A. (ed.), *Drought and Water Crises: Science, Technology, and Management Issues*, CRC Press (Taylor & Francis), Boca Raton 2005, pp. 389–398.
[29] Stagge J.H., Kingston D.G., Tallaksen L.M., Hannah D.M.: *Observed drought indices show increasing divergence across Europe*. Scientific Reports, vol. 7, 2017, 14045. https://doi.org/10.1038/s41598-017-14283-2.
[30] Dubrovský M., Hayes M., Duce P., Trnka M., Svoboda M., Zara P.: *Multi-GCM projections of future drought and climate variability indicators for the Mediterranean region*. Regional Environmental Change, vol. 14(5), 2014, pp. 1907–1919. https://doi.org/10.1007/s10113-013-0562-z.
[31] Sheffield J., Wood E.F.: *Projected changes in drought occurrence under future global warming from multi-model, multi-scenario, IPCC AR4 simulations*. Climate Dynamics, vol. 31(1), 2007, pp. 79–105. https://doi.org/10.1007/s00382-007-0340-z.
[32] Spinoni J., Naumann G., Vogt J.V.: *Pan-European seasonal trends and recent changes of drought frequency and severity*. Global and Planetary Change, vol. 148, 2017, pp. 113–130. https://doi.org/10.1016/j.gloplacha.2016.11.013.
[33] Spinoni J., Naumann G., Vogt J., Barbosa P.: *European drought climatologies and trends based on a multi-indicator approach*. Global and Planetary Change, vol. 127, 2015, pp. 50–57. https://doi.org/10.1016/j.gloplacha.2015.01.012.
[34] Dabrowska-Zielinska K., Malinska A., Bochenek Z., Bartold M., Gurdak R., Paradowski K., Lagiewska M.: *Drought model DISS based on the fusion of satellite and meteorological data under variable climatic conditions*. Remote Sensing, vol. 12(18), 2020, 2944. https://doi.org/10.3390/rs12182944.

[35] Gessner U., Reinermann S., Asam S., Kuenzer C.: *Vegetation stress monitor – assessment of drought and temperature-related effects on vegetation in Germany analyzing MODIS time series over 23 years*. Remote Sensing, vol. 15(22), 2023, 5428. https://doi.org/10.3390/rs15225428.

[36] European Commission, Joint Research Centre (JRC): *EDO Combined Drought Indicator (CDI) (version 4.1.0)* [dataset]. 2026. https://doi.org/10.2905/JRC.9QA0Z6R.

[37] Łągiewska M., Bartold M.: *An integrated approach using remote sensing and multi-criteria decision analysis to mitigate agricultural drought impact in the Mazowieckie Voivodeship, Poland*. Remote Sensing, vol. 17(7), 2025, 1158. https://doi.org/10.3390/rs17071158.

[38] Cammalleri C., Arias-Muñoz C., Barbosa P., de Jager A., Magni D., Masante D., Mazzeschi M., McCormick N., Naumann G., Spinoni J., Vogt J.: *A revision of the Combined Drought Indicator (CDI) as part of the European Drought Observatory (EDO)*. Natural Hazards and Earth System Sciences, vol. 21(2), 2021, pp. 481–495. https://doi.org/10.5194/nhess-21-481-2021.

Appendix 1

Table A1. Climate types according to the letter designations in the Köppen–Geiger classification

First letter		Second letter		Third letter	
Code	Description	Code	Description	Code	Description
B	dry climate/ desert	s	steppe climate (semi-arid); annual precipitation range between 380 and 760 mm	a	hot summer
C	hot moderate climate	f	wet climate: precipitation occur every month of the year, with no dry season	b	moderate summer
D	cold moderate climate	t	average temperature of the hottest month between 0 and 10°C	c	short and cold summer
E	Polar climate	f	average temperature of the hottest month below 0°C	k	dry and cold

Appendix 2

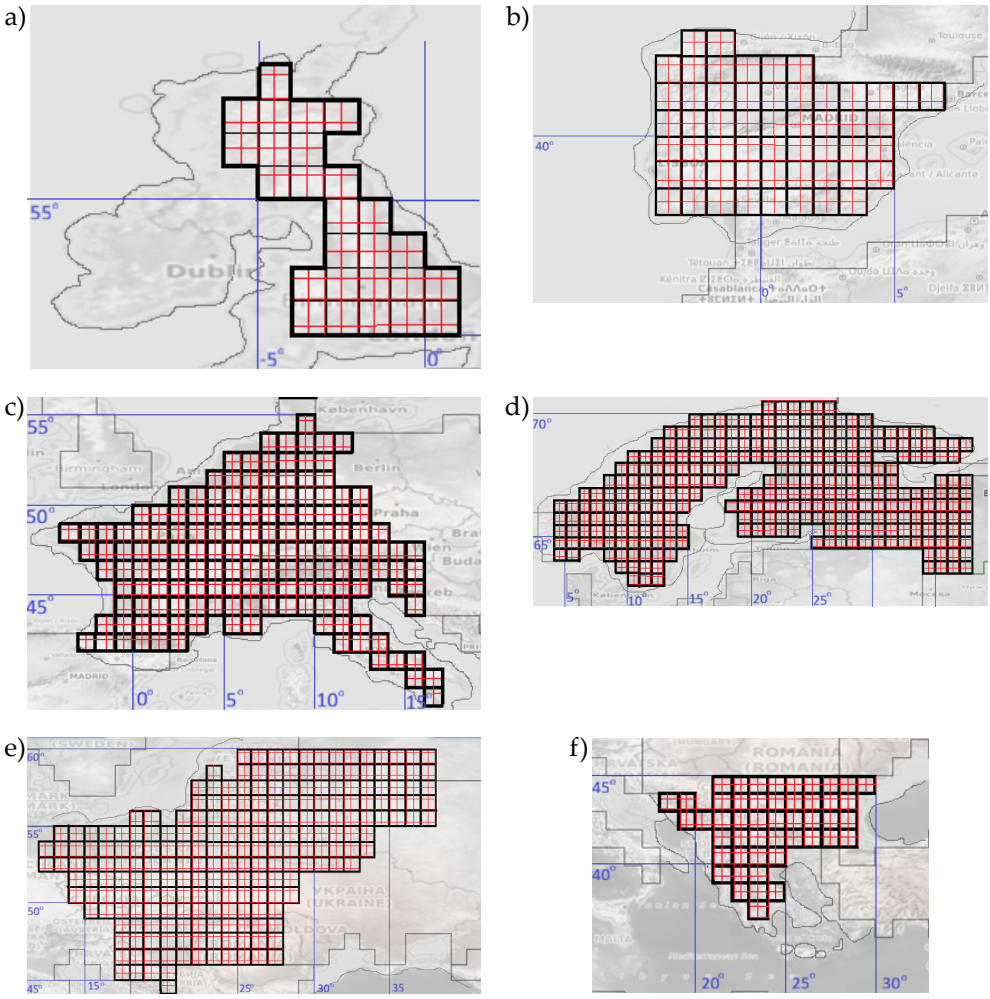

Fig. A2. Grids of GRACE TWS (black) and MERRA (red) for areas:
1 (a), 2 (b), 3 (c), 4 (d), 5 (e), and 6 (f)

Appendix 3

Table A3. Drought severity category

CCDI [cm]	WSDI [cm]	Drought severity category
(−∞, −1.44]	(−∞, −3]	extreme drought (D4)
[−1.45, −0.93]	[−3, −2]	severe drought (D3)
[−0.94, −0.45]	[−2, −1]	moderate drought (D2)
[−0.46, −0.28]	[−1, 0]	mild drought (D1)
[−0.29, 0.28]	[0, 0.5]	normal (N0)
[0.29, 0.45]	[0.5, 1]	mild wet (W1)
[0.46, 0.94]	[1, 1.5]	moderate wet (W2)
[0.95, 1.44]	[1.5, 2]	severe wet (W3)
[1.45, ∞)	[2, ∞)	extreme wet (W4)

Source: [22]

Appendix 4

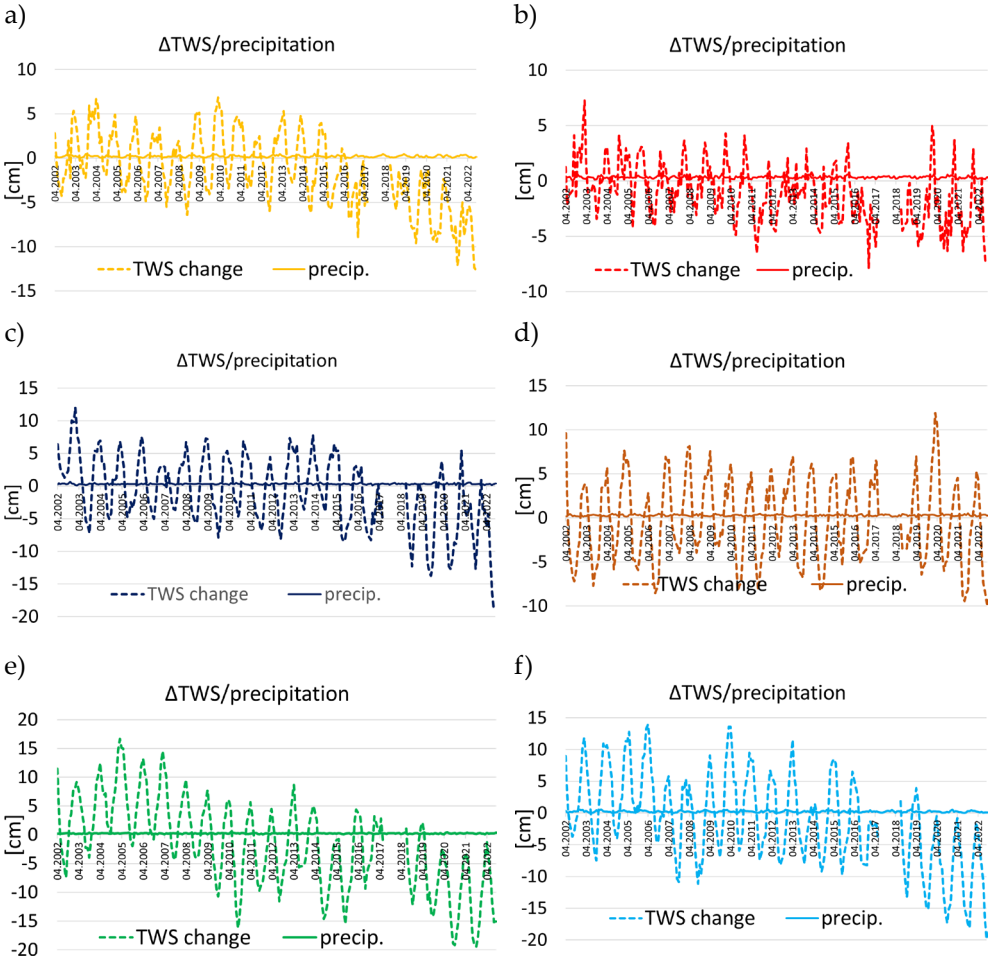

Fig. A4. Total water storage change and precipitation rate change for regions: 1 (a), 2 (b), 3 (c), 4 (d), 5 (e), and 6 (f)

Appendix 5

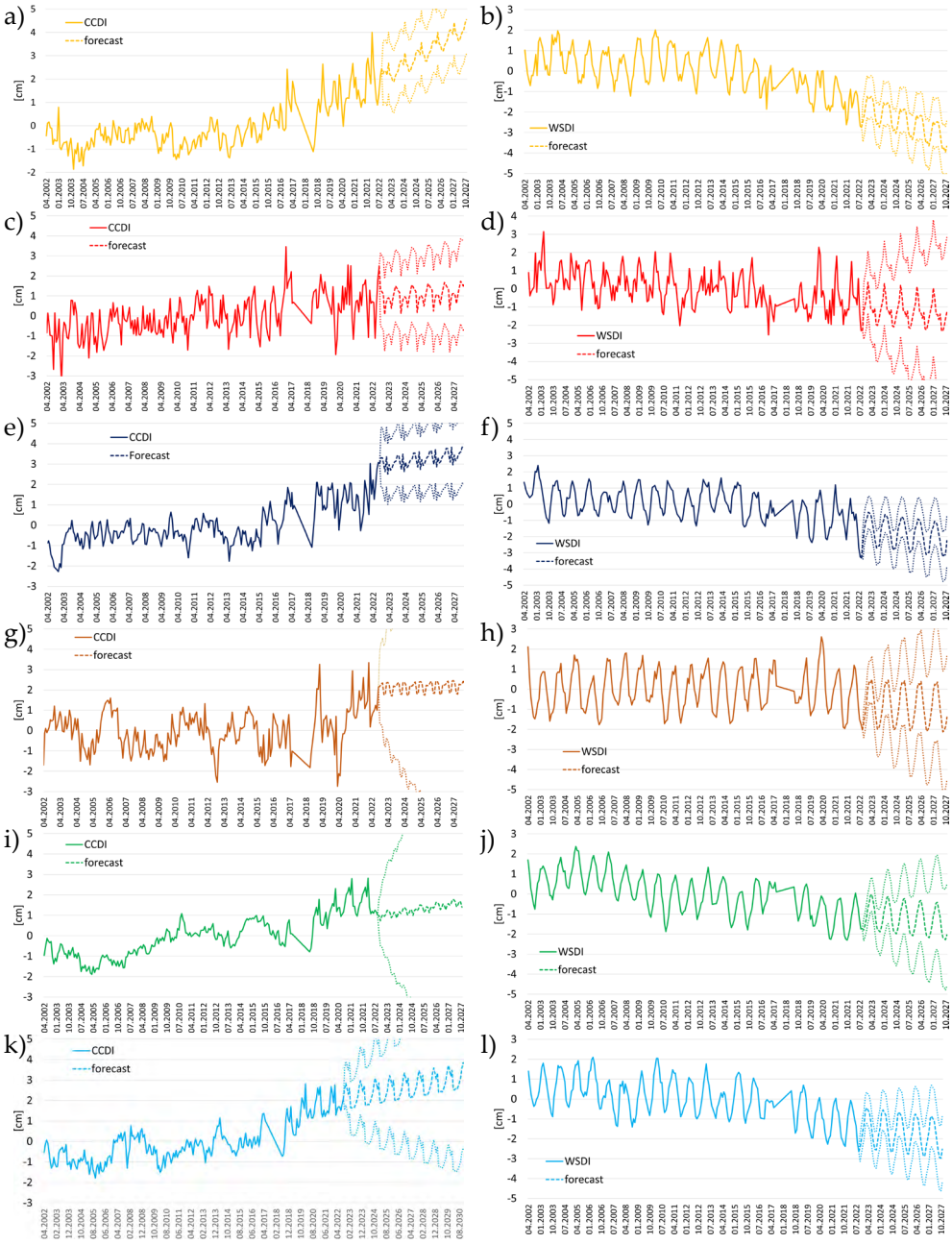

Fig. A5. Combined Climatological Deviation Index and its prognosis for 5 years and trend line for areas: 1 (a), 2 (c), 3 (e), 4 (g), 5 (i), and 6 (k).
Water Storage Deficit Index and its prognosis for 5 years and trend line for areas: 1 (b), 2 (d), 3 (f), 4 (h), 5 (j), 6 (l). All values in centimetres

Appendix 6

Table A6. Accuracy rating of ARIMA/SARIMA forecasts

Area	ADF (stat, *p*)	KPSS (stat, *p*)	AIC ARIMA	AIC SARIMA	BIC ARIMA	BIC SARIMA	Ljung–Box *p*
CCDI_1	–1.84, 0.35	0.92, 0.01	1,181	1,104	1,200	1,125	0.14
CCDI_2	–2.10, 0.24	1.04, 0.01	1,254	1,168	1,275	1,189	0.20
CCDI_3	–1.55, 0.48	1.21, 0.01	1,129	1,039	1,147	1,059	0.09
CCDI_4	–0.97, 0.79	1.30, 0.01	1,310	1,198	1,331	1,219	0.31
CCDI_4	–0.97, 0.79	1.30, 0.01	1,310	1,198	1,331	1,219	0.31
CCDI_5	–2.44, 0.13	0.88, 0.02	1,098	1,012	1,116	1,033	0.26
CCDI_6	–1.61, 0.45	1.18, 0.01	1,389	1,304	1,407	1,325	0.18
WSDI_1	–1.92, 0.33	0.95, 0.02	1,210	1,139	1,229	1,160	0.11
WSDI_2	–2.05, 0.27	1.09, 0.01	1,175	1,088	1,194	1,109	0.17
WSDI_3	–1.44, 0.52	1.28, 0.01	1,237	1,135	1,256	1,157	0.09
WSDI_4	–1.88, 0.36	0.99, 0.02	1,181	1,092	1,201	1,114	0.19
WSDI_5	–2.28, 0.16	0.90, 0.02	1,104	1,027	1,123	1,049	0.22